Soft Matter

View Online / Journal Homepage
Dynamic Article Links

Cite this: DOI: 10.1039/c2sm06740d

www.rsc.org/softmatter

PAPER

Electrically conductive polymeric photonic crystals†

Yusuke Imai,‡*[a] Chris E. Finlayson,§*[a] Pola Goldberg-Oppenheimer,[a] Qibin Zhao,[a] Peter Spahn,[b] David R. E. Snoswell,[a] Andrew I. Haines,[a] G. Peter Hellmann[b] and Jeremy J. Baumberg*[a]

Received 13th September 2011, Accepted 24th April 2012
DOI: 10.1039/c2sm06740d

Downloaded by University of Cambridge on 08 May 2012
Published on 08 May 2012 on http://pubs.rsc.org | doi:10.1039/C2SM06740D

Electrically conductive polymeric 3D photonic crystals are prepared by the shear ordering of composites consisting of monodisperse core-shell polymer spheres and single-walled carbon nanotubes (SWNTs). Strong iridescent colour indicates that the highly ordered opaline structures are not disrupted by the presence of the conductive nanotube networks. Thermal annealing leads to a significant increase in the overall electrical conductivity of thin-film samples yielding DC conductivities of 10^{-4} S cm^{-1}, with percolation thresholds of less than 0.4 wt% of SWNT. Such composites with open networks of carbon nanotubes held apart by lattices of hard spheres, give combined conductive properties and structural colour effects, within a tuneable viscoelastic medium, with many potential functional applications.

Introduction

Colloidal crystals have attracted much attention in recent years, as examples of photonic structures, where periodic variations in refractive index create photonic band-gaps. Within these band-gaps, the propagation of a certain wavelengths of light is prohibited,[1] and a range of novel optical properties such as structural colour,[2] "slow-light"[3] and "superprism"[4] effects are possible. Photonic crystal principles allow development of structured materials with distinguishing optical properties, which are not accessible using dyes or pigments. Colloidal crystals can be fabricated by self-assembly of sub-micron sized monodisperse spheres, typically made of polystyrene or silica.[5,6] Layers of close-packed spheres generate the periodic refractive index change and the maximum wavelength of reflection λ_{max} from the colloidal crystal is given by the well-known Bragg equation, where d is layer spacing, n_{eff} is effective refractive index, and θ is incident angle.

$$\lambda_{max} = 2d\sqrt{n_{eff}^2 - \cos^2\theta} \qquad (1)$$

In recent work, we have reported three-dimensional (3D) ordered polymeric photonic crystal or polymer opals.[7–17] These are fabricated by shear-induced ordering of core-interface-shell (CIS) structured polymer spheres. The CIS polymer sphere is composed of a rigidly cross-linked polystyrene core (*i.e.* a rigid spherical core) covered with a low-glass transition temperature (T_g) poly(ethyl acrylate) (PEA) soft shell, *via* a thin (~10 nm) poly(methyl methacrylate) interlayer containing the co-monomer allyl methacrylate (ALMA) as a grafting agent (Fig. 1a). Synthesis of CIS spheres is achieved by an emulsion polymerization route and the overall CIS diameter is readily controllable, typically ranging from 150 to 350 nm, without affecting the high monodispersity.[15,18] The Bragg wavelength can be tuned over the whole range of the visible and near infrared spectral region by adjusting the sphere size. The soft shell polymer forms a continuous matrix during the shear-ordering process and the rigid spheres become regularly arranged in this matrix. The net refractive index contrast between core and shell materials in the archetypal PS/PEA system is $\Delta n \approx 0.11$, with $n_{eff} \approx 1.51$. Doping polymer opals with tiny amounts of carbon nanoparticles causes a dramatic enhancement of the resonant Bragg scattering and gives significant color enhancement and a peculiar angular dependence.[11] A recently developed edge-induced rotational shearing (EIRS) process has been shown to induce 3D opaline ordering of CIS spheres over areas of 10s of square-centimeters and through film thicknesses of greater than 100 microns.[14] The exceptional flexibility and stretchability (>100%) of the final polymer opal, along with the possibility of tuning the optical properties by deformation,[13,15] render this structure as a rather unique photonic crystal. However, the prospects for utilising such photonic materials in optoelectronic applications, such as photovoltaics or electrically-tuneable colour films, require conductive colloidal crystals which have been unavailable thus far.

---

[a] *Cavendish Laboratory, University of Cambridge, Cambridge CB3 0HE, UK. E-mail: jjb12@cam.ac.uk; Fax: +44 1223 764515; Tel: +44 1223 760945*
[b] *Deutsches Kunststoff-Institut (DKI), Darmstadt D-64289, Germany*

† Electronic Supplementary Information (ESI) available: details of sample preparation, optical & electronic characterisation, and electron microscopy. See DOI: 10.1039/c2sm06740d/

‡ Current Address, National Institute of Advanced Industrial Science and Technology (AIST), Advanced Manufacturing Research Institute, Nagoya 463-8560, Japan. y-imai@aist.go.jp

§ Current address: Institute of Mathematical and Physical Sciences, Prifysgol Aberystwyth University, Aberystwyth SY23 3BZ, Wales UK. cef2@aber.ac.uk

Downloaded by University of Cambridge on 08 May 2012
Published on 08 May 2012 on http://pubs.rsc.org | doi:10.1039/C2SM06740D

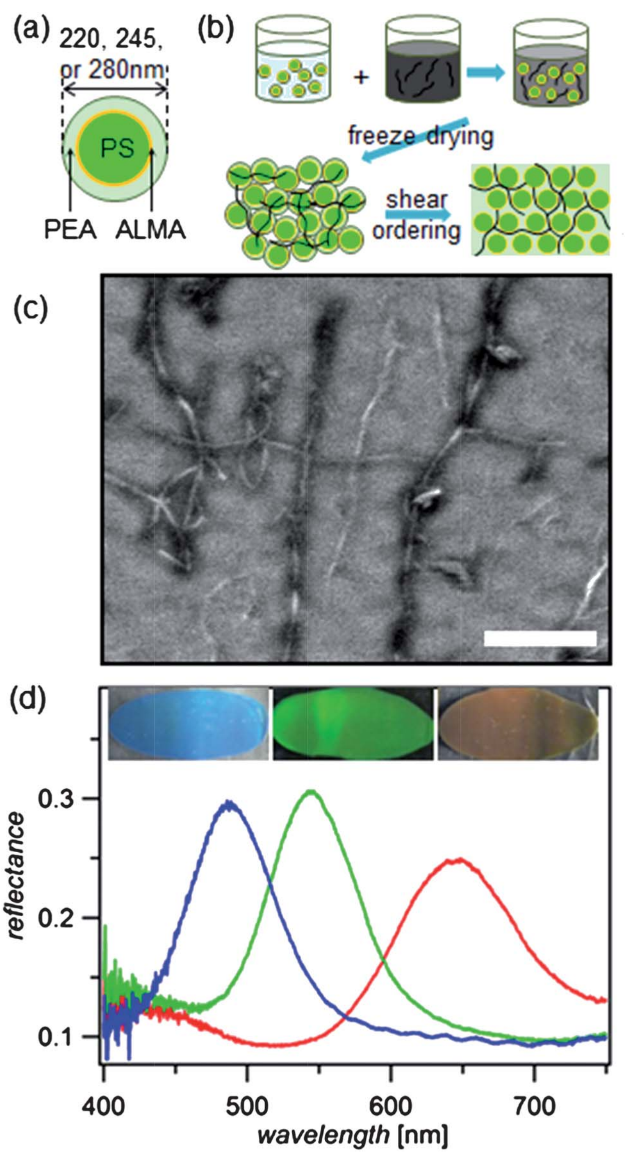

Fig. 1 (a) Core-interlayer-shell (CIS) structure of the constituent particles used to form polymer opals. (b) Schematic of preparation procedure of SWNT-doped polymer opals. (c) SEM image of an annealed opal with 1wt% SWNT. The scale bar is 500 nm. (d) Reflection spectra of SWNT (0.1wt%)-doped polymer opal films from three different sized CIS particles. The noticeably broader width of the red opal spectrum is due to the inverse scaling of the wavelength with energy. Inset: photographs of the as-prepared films, as viewed in reflected white light.

In the present study, we demonstrate 3D polymeric photonic crystals, which are rendered electrically conductive by forming a nanocomposite with carbon nanotubes.

Single-walled carbon nanotubes (SWNTs) have diameters of 1–2 nm and lengths of up to several microns.[19]The exceptional mechanical, thermal and electrical properties of SWNTs have driven many studies in a whole range of research fields. The use of SWNTs as fillers in polymer matrixes, predominantly aiming for mechanical reinforcement or improvement of the nanocomposite electrical properties, has been widely exploited to generate advanced high-performance materials and devices.[20–29] However, very little work has been reported on incorporating such conductive SWNTs into optical materials based on photonic crystal structures. Furthermore, the required dispersion and partial aggregation of the nanotubes to form a conducting network in a dilute medium (such as a polymer matrix) is non-trivial, as the energetics of mixing will be different for each polymer system.

The conductive polymeric opals reported here are comprised of monodisperse core-shell polymer spheres surrounded by SWNTs. Optically, these structures exhibit a strong iridescent color, indicating that the highly ordered opaline structures are not disrupted by the presence of the nanotube networks. Thermal annealing is found to have a significant effect on the electrical conductivity of thin-film samples, which is further analyzed using impedance spectroscopy, electron microscopy of the composite microstructure, and by studying the mechanical properties of thin-films (Young's modulus). DC conductivities of the order of 10^{-4} S cm^{-1} are achieved, with percolation thresholds of less than 0.4 wt% of SWNT. Our approach provides a distinctive route to combine the attractive optical properties of opaline photonic crystals with intrinsic electroactivity. These *direct opal* structures have a number of attractive features, when compared to examples of conducting/semiconducting inverse opals,[30,31] such as inherent optical tunability due to viscoelasticity. Such functionality can potentially lead to the generation of high-performance integrated nanodevices.

Experimental methods†

The production of SWNT-doped polymer opals is schematically illustrated in Fig. 1b and a representative sample, as fabricated, is shown in Fig. 1c. In order to incorporate SWNTs into the interstices of 3D photonic crystal lattice, where the narrowest distance between neighbouring core spheres is only several tens of nanometres, the SWNTs and CIS polymer spheres must firstly be prepared in a homogeneously dispersed state.[25,26]

For our experiments, SWNTs were purchased from Carbon Solutions Inc., (P2-SWNT grade), with a carbonaceous quality of >90% and typical lengths of order 100–1000 nm. An aqueous dispersion of the SWNTs was prepared by using the anionic surfactant sodium dodecylbenzenesulfonate (SDBS) as a stabilizing agent. A stable dispersion of SWNTs was obtained *via* ultrasonication, followed by subsequent centrifugation. Three different sized CIS polymer spheres, with mean diameters of 220, 245, and 280 nm were used to fabricate SWNT-based polymer opals. Using high-resolution hydrodynamic chromatography, spheres were typically found to have a coefficient of variation (ratio of standard deviation in diameter to the diameter itself) of 0.1 or better.[18] The spheres, as synthesized by an emulsion polymerization process, are colloidal dispersed in an aqueous medium. These two kinds of dispersions were mixed in specific ratios, so that the weight concentration of SWNT to polymer spheres could be controlled in the range from 0.1 to 1.0 wt%. The mixture did not produce any precipitates upon mixing and formed a stable and homogeneous mixture. Next, the water was removed from the mixtures by freeze-drying, in order to avoid phase separation during the drying process. It was found that removal of water by heating caused sedimentation of the SWNTs and, as a result, the product was inhomogeneous. By employing the freeze-drying method, homogeneous compounds without

This journal is © The Royal Society of Chemistry 2012

Published on 08 May 2012 on http://pubs.rsc.org | doi:10.1039/C2SM06740D
Downloaded by University of Cambridge on 08 May 2012

apparent phase separation have been obtained. The SWNT/polymer sphere composites were then processed by rolling (applying linear shear) and, subsequently, an edge-induced rotational shearing process.

Details of these processes and the effectiveness for full 3D ordering of CIS spheres are described in our recent report.[14] Film samples with thickness of approximately 100 μm were prepared *via* this process. Further details are also given in the *Supplementary Information* section of this paper.† The effect of thermal annealing was studied by subsequently heating the sample films at 140 °C in air for periods of up to 4 h. These annealing procedures have a direct impact on both the morphological and the conductive properties of the nanocomposite opals as discussed in more detail in the following sections.

Results

Characterization; optical and morphological properties

Representative photographic images under white light of the as-prepared films (Fig. 1d inset) show brilliant structural colors of blue, green and red, for samples using 220, 245 and 280 nm spheres, respectively. Reflection spectra (Fig. 1d) show intense peaks centred at $\lambda = 487$, 544, and 646 nm respectively, which correspond to the normal incidence resonant Bragg reflection.[16] These reflection peaks are clearly indicative of the highly regular ordering of the polymer opal structure having been retained,[12,14] in spite of the doping with SWNT, due to their insertion into the soft shells of the particles and the relatively low doping concentration.

Microtomed cross-sections perpendicular to the film surface, examined by transmission electron microscopy (TEM) and scanning electron microscopy (SEM), yield insights into the SWNT distribution inside the polymer opal structure and their morphological organization. Cryo-microtoming of these samples, to thicknesses of the same order as the sphere diameters, inevitably results in some distortion of the opaline lattices; however the presence of nanotube bundles in the interstices between spheres can be qualitatively seen. Fig. 2 reveals well-dispersed SWNTs incorporated inside the polymer opal structure prior to (Fig. 2a,b) and after (Fig. 2c,d) samples are annealed at 140 °C for 1 h in air. Discreet bundles of SWNTs, which are the result of the colloidal mixing and freeze drying processes, can be observed in Fig. 2a. Since thin TEM cross-sections provide only two-dimensional imaging, which gives limited information regarding the SWNT organization inside the opaline matrix, SEM examination provides an additional view of their morphological organization. The inset in Fig. 2b reveals SWNTs organized in a "snake"-like geometry, with some conformity to the contours of the PS spheres. A closer examination reveals individual SWNTs preferentially located in the voids between the adjacent PS spheres (Fig. 2d, inset). Therefore we conclude that CNTs are indeed excluded from the PS cores and reside within the PEA shell in the sphere interstices.

Annealing procedures have a direct impact on the conductive properties of the nanocomposite opals. Electrical conductivities of as-prepared samples before annealing were found to be fairly low even at high SWNT concentrations, indicating that electrical connection among SWNTs is initially limited after the assembly process. From previous reports, we expect that the surfaces of the dispersed SWNTs are fully covered by surfactant molecules, which adsorb through hydrophobic and π–π interactions between the dodecylbenzene group of SDBS and the graphenic surface of SWNT.[32]Annealing at 140 °C was chosen because it is (a) below the oxidation temperature of SWNTs, and (b) also somewhat below the EIRS processing temperature (thus preventing opal lattice reorganisation), yet (c) above the lowest temperatures needed for modifying the dispersing surfactant (~50 °C) which results from loss of water content from the SDBS.[33] Following the thermal annealing process, SWNTs appear in TEM with higher image contrast (Fig. 2c,d), which is also ascribed to these changes in the SDBS coating. The visible emergence of SWNTs at the surface after heat treatment and the apparent randomisation of the bundle orientation (*cf.* Fig. 2a,c) are further indications of reorganisation/removal of SDBS in the SWNTs nanocomposites. Current models of surfactant action suggest their hydrophobic groups wrap and stabilize the nanotubes, while their hydrophilic groups decrease the surface tension between adjacent CNTs and efficiently stabilise them.[34–36] This non-covalent surfactant adsorption is known to limit the flow of electrons among nanotubes, resulting in poorer conductivity of SWNTs. Annealing treatments at temperatures above the initial modification point of the organic surfactant and lower than that of SWNTs can overcome this intrinsic limit to conductivity. Local reorganisation and/or removal of the organic groups surrounding the nanotubes while retaining the integrity of the SWNT bundles, thus decreases the contact resistance between CNTs and consequently improves the conductive properties of the whole film.[37]In previous work on CNT/polymer composites, processes such as shear-alignment,[38]scission,[39] and thermal annealing[40] have been reported to have a profound effect on the morphologies of mixing and on nanotube connectivity, as reflected in changes to the observed bulk electrical properties. However, annealing of our samples at 140 °C did not cause any destruction of the opaline structure (Fig.2) or the inferred SWNT lengths, although it is found to have a very marked effect on the conductive properties.

We do not have an independent confirmation of the exact thicknesses of the surfactant layers, as deposited on the SWNTs. However, as a first-order estimate, we expect that the thickness of the adsorbed layer is of the order of the fully extended length of the surfactant molecules. For most commonly used surfactants, this thickness is 2–4 nm.[41]

For the more detailed studies of optical and electrical properties of thin-film samples with different SWNT concentrations we focus in the remainder of this paper on green opals with 245 nm CIS spheres, with all subsequent annealing treatment being carried out at 140 °C in air. Fig. 3 shows reflectance spectra of the as-prepared films with different SWNT concentrations. All the samples show sharp peaks in reflectance (Fig. 3a), indicating the excellent ordering of spheres, even with higher concentrations of SWNT. The color of the sample films becomes darker with higher concentration of SWNT (Fig. 3a inset) due to the SWNT absorption, but the green color can be clearly identified for each composition. Strong absorption by SWNTs reduces reflection peak amplitudes and the peaks also show a red-shift with increasing SWNT concentration. This latter effect is a consequence of photonic band-gaps and standing waves. On the red

Downloaded by University of Cambridge on 08 May 2012
Published on 08 May 2012 on http://pubs.rsc.org | doi:10.1039/C2SM06740D

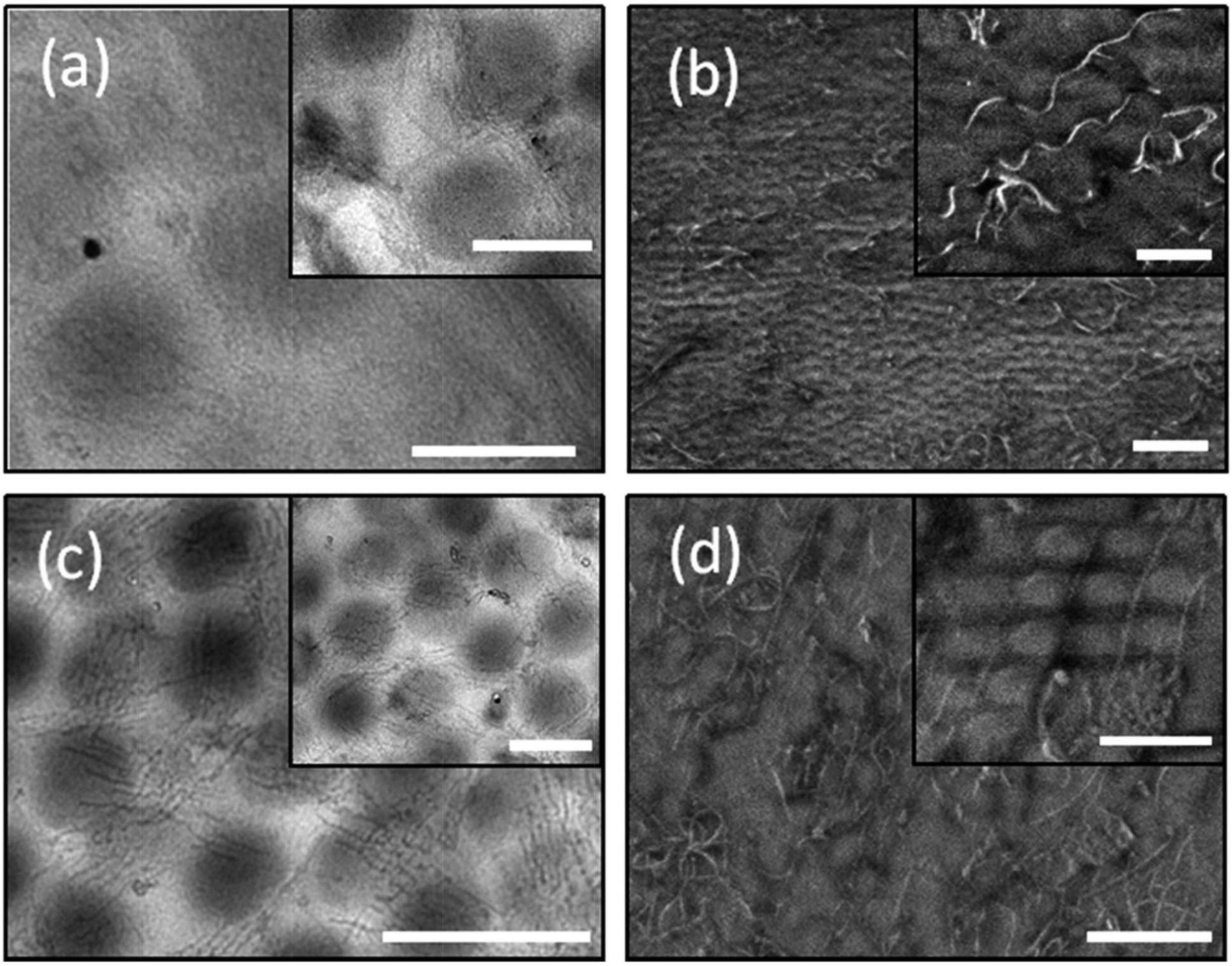

Fig. 2 (a) and (b) show TEM and SEM images respectively of an unannealed green opal film with 1%wt SWNT. (c) and (d) show corresponding TEM and SEM images of the sample after annealing at 140 °C for 1 h. The scale-bars have lengths corresponding to 250 nm (inset 250 nm) in (a), 1000 nm (inset 500 nm) in (b), 500 nm (inset 250 nm) in (c), and 1000 nm (inset 500 nm) in (d).

(low energy) side of the Bragg resonance the light is located within the high refractive index cores, while on the blue side the light is in the low refractive index surroundings where the SWNTs are located. Increasing the absorption in the low *n* medium attenuates the blue side of the resonances, which effectively shifts the resonance towards the red. According to theory, the maximum red shift due to this effect is one half-linewidth,[7] which is what is observed. Reflectance spectra (Fig. 3b) show a slight reduction in amplitude with annealing, but the peak width does not change. Additionally, the peak position shifts slightly to shorter wavelengths during annealing, indicating that a small relaxation of the processing-induced strain in the CIS sphere array takes place. However, the structural colour features are maintained, and the regular 3D ordering of spheres is demonstrably preserved.

Electrical impedance spectroscopy

In order to gain a more complete understanding of the physical properties of our SWNT/polymer-opal composites, and of issues such as the continuity and morphology of the nanotube network,[27] electrical impedance spectroscopy measurements were performed on a series of thin-film samples, under different preparation and annealing conditions.

The frequency dependence of the conductivity, σ, and real-part of the dielectric constant, ε_r, for samples with different SWNT densities, ρ, in units of percentage by weight is shown in Fig. 4. The thicknesses and planar areas of all samples are measured to allow the raw conductivity and capacitance data to be converted into intensive units. At low values of ρ, the samples show $\sigma < 10^{-10}$ S cm^{-1} (below our detection limits) at low frequency (Fig.4a) and $\varepsilon_r \sim 3$, which is independent of frequency (Fig.4b). This is what would be expected for a non-conducting dielectric layer. The conductivity of samples after annealing at 140 °C for 1 h is seen (in Fig.4a,c) to significantly increase for all values of ρ, by up to three orders of magnitude. After annealing, spectra now have a measurable DC conductivity, with values in the range of 10^{-5} to 10^{-4} S cm^{-1}. There is also a change (Fig.4b,d) in the functional form of $\varepsilon_r(\omega)$; in the annealed samples, there is a distinct plateau in the spectrum at low frequency, which is characteristic of the behavior of parallel circuits with conductive and capacitive components.[40,42] Of further interest is the apparent lack of dependence on the processing conditions, *i.e.* whether or not samples had been edge-sheared to produce higher

This journal is © The Royal Society of Chemistry 2012

Downloaded by University of Cambridge on 08 May 2012
Published on 08 May 2012 on http://pubs.rsc.org | doi:10.1039/C2SM06740D

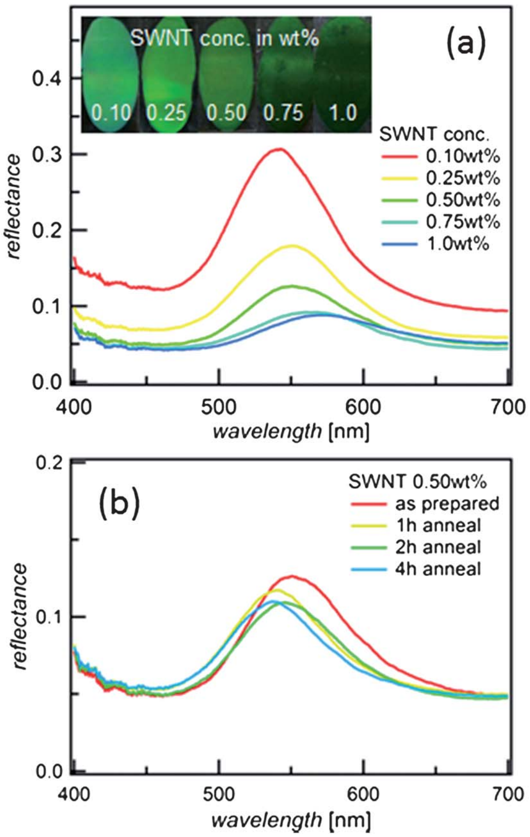

Fig. 3 (a) Reflection spectra of as-prepared samples with different SWNT concentrations. Inset: photographs of the samples. (b) Change of reflection spectra with annealing at 140 °C.

opaline ordering. This suggests that there is no scission effect or preferential directionality of the nanotube network in the shear process.

To undertake more detailed analysis, the frequency dependence of real and imaginary impedance (Z' and Z'') are extracted to give information about the cross-over from non-conductive to conductive behavior below a cut-off frequency, f_0. Using impedance spectroscopy measurements different length scales within the sample can be probed as the modulation frequency is varied. The characteristic length scale of the conductive network is associated with the effective distance between junctions in the SWNT networks; this length is probed when it is comparable with the AC modulation period, thus allowing charges to travel from one junction to another along the SWNT bundles. At frequencies $f < f_0$, the charge carriers percolate over larger distances, becoming comparable to the scale of the entire nanotube network in the low frequency limit, where the impedance is then equivalent to the DC resistance of the network. For $f > f_0$, the carriers percolate over a shorter distance within each AC cycle, with carriers only tending to move within bundles. A transition from long-range transport to localized carrier confinement is characterized by a cut-off frequency in Z', and is also correlated with a maximum in Z''. In Fig. 5a, $Z'(\omega)$ and $Z''(\omega)$ are shown for a representative sample, annealed for 1 h at 140 °C, illustrating how f_0 values can be clearly extracted from the data. In Table 1, f_0 values are tabulated as a function of the length of time of annealing, at a fixed temperature. The clear trend shows f_0 shifting to higher frequencies as the annealing time is increased, whilst the unannealed samples show no clear cross-over to conducting behavior. As ρ increases, f_0 also clearly shifts to higher frequencies, and the real impedance correspondingly decreases. This is consistent with the increased levels of connectivity between nanotubes and changes to the *effective* lengths between junctions, in addition to the issues of contact resistance, as already discussed.

To gain a better insight into the microscopic electronic transport, the correlation between the SWNT density, ρ, and the conductive properties are analyzed in more detail. In Fig. 6a, the variation of the extrapolated DC conductivity, σ_{dc}, with ρ is shown for samples prepared with various annealing times. There is a clear contrast between unannealed samples, where there is relatively weak variation in σ_{dc} with increasing ρ, and annealed samples, where a *critical behavior* is seen and the conductivity increases by many orders of magnitude above a certain density threshold, ρ_0. To better quantify this critical threshold, the data is fit to a generic sigmoidal function,

$$\sigma_{dc}(\rho) = A + \left[\frac{B}{1 + \exp\left(\frac{\rho - \rho_0}{C}\right)}\right] \tag{2}$$

The resultant values of ρ_0 were 0.84(±0.24) wt% for the unannealed sample, 0.39(±0.01) wt% for 1 h anneal, 0.38(±0.02) wt% for 2 h and 0.39(±0.02) wt% for 4 h. Hence, we conclude that the annealed SWNT networks have similar critical densities of ~0.39wt%. Whilst these values are lower than many reported for CNT/soft-polymer composites, we note that in our system the nanotubes are excluded from the rigid polystyrene cores and reside within the PEA shell material in the interstices (see Fig. 2a,b). Hence the *local* density of SWNTs is approximately twice as high in this shell material as in the bulk sample as a whole.

As described in an earlier section, the peak reflectivities of samples decrease, as the doping fraction of SWNTs increases. This clearly presents a trade-off between samples having high conductivity or high reflectivity. However, we emphasize that at the percolation threshold of $\rho_0 \approx 0.4\%$, samples still exhibit a marked structural colour, with the subjective appearance being particularly vivid (Fig. 3a), as much of the background scattering is absent as compared to undoped samples. In the future, we anticipate that subsequent optimization of processing parameters will enable us to further reduce ρ_0 towards lower values, thus also enabling very high reflectivity from conductive samples.

Above ρ_0, the variation in conductivity is expected to follow a power-scaling law:

$$\sigma(\rho) = A(\rho - \rho_0)^{\beta}, \tag{3}$$

where A is constant and the exponent β relates to the dimensionality of charge transport. A value of $\beta \approx 1.3$ is expected for uniform two-dimensional transport and $\beta \approx 1.9$ for a three-dimensional case.[43,44] In Fig. 6b, fitting of the available data points for the samples annealed for 1, 2 and 4 h is shown, together with inferred β values. Whilst the low number of data points implies a 10% error in β, the data suggests that transport is not perfectly isotropic in 3-D, but is intermediate between 2- and 3-dimensionalities. Physically, this is likely to be because the

Downloaded by University of Cambridge on 08 May 2012
Published on 08 May 2012 on http://pubs.rsc.org | doi:10.1039/C2SM06740D

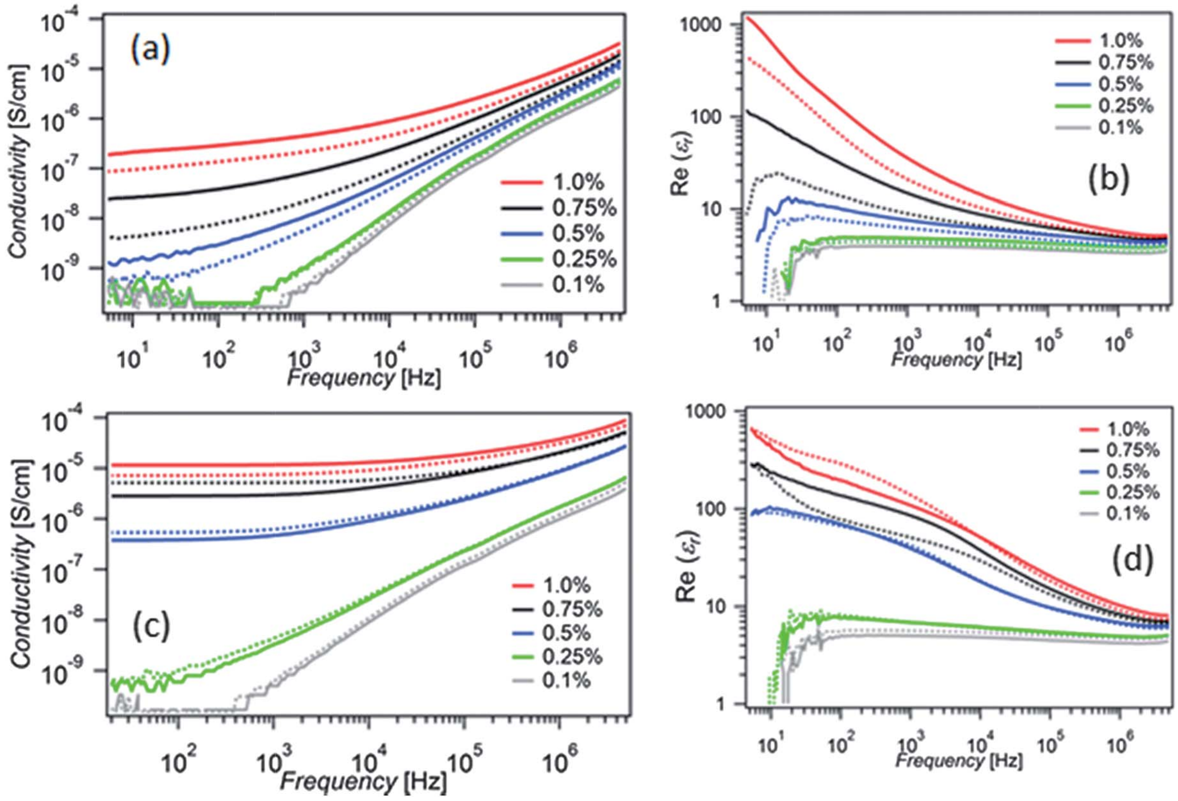

Fig. 4 Impedance spectroscopy data for films of SWNT/green polymer-opal composites, converted to conductivity and real part of the dielectric constant. In (a, b) the data for unannealed samples is shown, for different SWNT percentage by weight, as indicated. Solid lines represent samples which had been edge-sheared (opal-ordered) prior to measurement and dashed lines those which had not. Equivalent data is shown in (c, d) for samples which had been annealed at 140 °C for 1 h.

SWNT bundles are not randomly distributed in the bulk matrix, but must instead conform to the lattice geometry of the opal environment, hence residing in the interstices between spheres.

For a microscopic model of the electronic transport, a detailed analysis of the impedance properties of the composite samples considers the resistive and capacitive components of the network, in terms of bundles of SWNTs and of the junctions formed between them. For consistency edge-processed thin-film samples with similar thicknesses of ~100μm are used throughout the following analysis. Firstly, using a *single Voigt element* model (resistance R and capacitance C in parallel), we attempt to fit the impedance data, $|Z|$, to the standard expressions for $Z'(\omega,R,C)$ and $Z''(\omega,R,C)$, *i.e.*

$$Z' = Re\ (Z) = \frac{R}{1+\omega^2R^2C^2} \tag{4}$$

$$Z'' = Im\ (Z) = \frac{\omega R^2 C}{1+\omega^2R^2C^2}, \tag{5}$$

where $|Z|^2 = (Z')^2 + (Z'')^2$. The product RC is the relaxation time, τ, of the circuit and the cut-off frequency, $f_0 = 1/\tau$. An example of such a fit is shown in Fig. 5a. Typically we find that the peak in the Z'' spectrum is considerably broader than that predicted by this model, together with a broader transition from the non-conducting to conducting regime at f_0 in the Z' data. These differences indicate that the system has a much wider range of circuit relaxation times than for a simple single RC model. The physical interpretation of this is that the SWNT network has a distribution of different circuit elements and conductive pathways, which contribute to the overall resistance and capacitance of the film. In order to describe such a system quantitatively, and to develop a more general treatment of the R and C components of the system, we adopt the approach of Kirkwood and Fuoss,[42,45] where $Z''(\omega)$ is fit using a hyperbolic-secant function. The standard Debye model has a functional form

$$Z''/Z''_{max} = \text{sech}\ x, \tag{6}$$

where $x = \log\ (\omega/\omega_0) = -\log(f_0/f)$. In the modified situation presented here,

$$Z''/Z''_{max} = \text{sech}\ \alpha x, \tag{7}$$

where the parameter α is a measure of the broadness of the relaxation time distribution, where lower α implies a broader distribution about the mean relaxation time. In Fig. 5b, such fitting is applied to the data for the samples annealed for 1 h, with ρ values ranging from 0.5 to 1.0 wt%. We find that eqn (7) gives excellent fits to the data, with evidence of a broadening distribution of relaxation times with increasing ρ.

For samples with extended annealing times of 2–4 h, a distinct bimodal distribution in relaxation times becomes evident, as seen more clearly by plotting $Z''(\omega)$ on a log scale (Fig.5c). Whilst the reduction in the overall film resistance with annealing causes f_0 to

This journal is © The Royal Society of Chemistry 2012

Downloaded by University of Cambridge on 08 May 2012
Published on 08 May 2012 on http://pubs.rsc.org | doi:10.1039/C2SM06740D

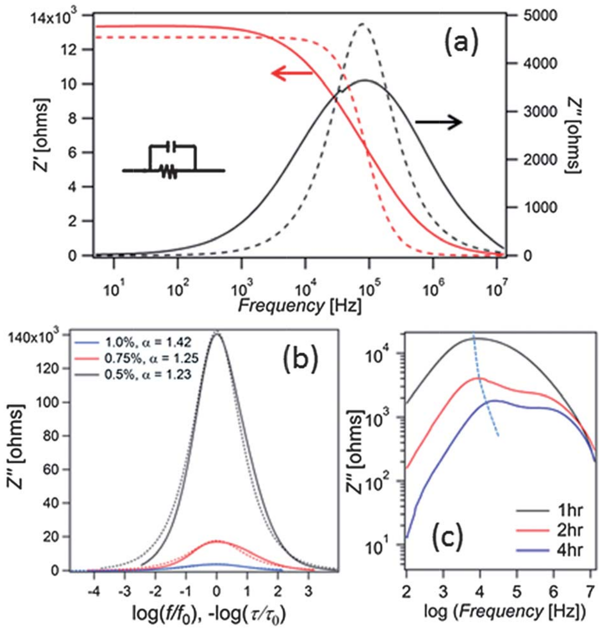

Fig. 5 (a) Frequency dependence of real and imaginary parts of impedance, for green opal sample with 1 wt% SWNT, annealed at 140 °C for 1 h. Fitting curves are shown (dashed) for both Z' and Z'', based on a single Voigt element model (inset). This global fitting gives $R = 13.0$ kΩ and $C = 3.24 \times 10^{-10}$ F, hence a cut-off frequency ~250 kHz. (b) Fitting of data using eqn (7) for samples annealed for 1 h. SWNT wt% concentrations as indicated and fits from which the parameter α is derived are shown as dashed lines. All the plots are re-normalised to have a common origin, based on the f_0 values reported in Table 1. (c) Imaginary $Z(\omega)$ on a log scale for a 0.75 wt% SWNT film, for different annealing times, as indicated. The locus (dashed line) shows the change in the position of the principal cut-off frequency (f_0) with increasing anneal time. A second peak at higher frequency peak (low relaxation times) becomes clear after annealing for >2 h.

shift to higher frequencies, a second peak at even higher frequency (lower relaxation times) appears. For this data, a more appropriate bimodal fitting function is the sum of two sech functions:

$$Z''/Z''_{max} = A \operatorname{sech} \alpha_1 x + B \operatorname{sech} \alpha_2 (x - c), \tag{8}$$

where α and x have the same meaning as previously, A and B are empirical constants, and c is a frequency offset, with $c = \log f_0 - \log f_0'$, where f_0 and f_0' are the cut-off frequencies associated with the primary and secondary (high frequency) peaks respectively. In Fig. 7 the data for $Z''(\omega)$ is fit to eqn (8) for a range of different ρ and annealing times. In contrast to the simpler model, good fits are now achieved for the samples with 2 h and 4 h anneal times. The fitted values of f_0 and c can be used

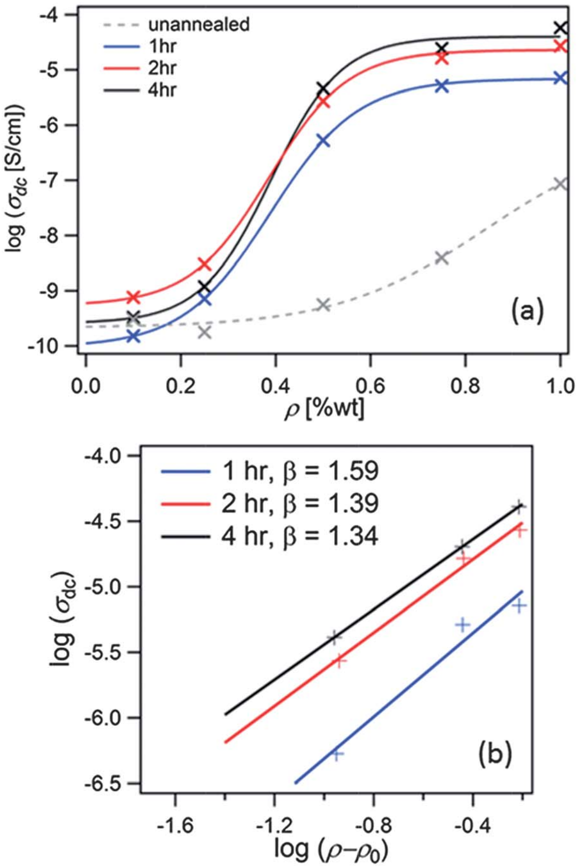

Fig. 6 (a) DC conductivity (log scale) as a function of SWNT density, in units of percentage weight. The graph shows data points for both unannealed and annealed green opal samples, as indicated. Lines of best fit to eqn (1) are also shown. (b) Using a log-log scale, DC conductivity is plotted against the parameter $\rho - \rho_0$ (SWNT density minus the critical densities derived from (a)), for different annealing times. The lines of best fit are derived from eqn (2), giving the values of co-efficient β, as indicated. Annealing temperature was 140 °C in all cases.

Table 1 Key parameters extracted from impedance spectroscopy models for green opal samples with varying SWNT weight fraction and annealing times. The mean values of resistances $R_{1,2}$ and capacitances $C_{1,2}$ are based on a bimodal distribution of relaxation times, as described in eqn (8); f_0' is the cut-off frequency associated with the secondary peak in the distribution at low relaxation times

SWNT wt (%)	Annealing time (hr)	f_0 (kHz)	f_0'(kHz)	Z ($f = 0$)	R_1 (ohms)	R_2 (ohms)	C1 (F)	C2 (F)
0.5	1	7.73	—	442000	431150	10850	3.00×10^{-10}	—
0.5	2	42.3	686	58200	57200	1000	4.13×10^{-10}	1.45×10^{-9}
0.5	4	98.3	1154	35700	35095	605	2.9×10^{-10}	1.43×10^{-9}
0.75	1	42.0	593	60900	59704	1196	3.99×10^{-10}	1.41×10^{-9}
0.75	2	70.8	2754	14600	14433	167	9.79×10^{-10}	2.17×10^{-9}
0.75	4	225	5651	7030	6957	73	6.39×10^{-10}	2.42×10^{-9}
1.0	1	236	—	13350	13053	297	3.24×10^{-10}	—
1.0	2	364	10259	3710	3652	58	7.52×10^{-10}	1.68×10^{-9}
1.0	4	669	15325	2650	2614	36	5.72×10^{-10}	1.81×10^{-9}

Downloaded by University of Cambridge on 08 May 2012
Published on 08 May 2012 on http://pubs.rsc.org | doi:10.1039/C2SM06740D

to extract further information about the circuit elements in these thin-film samples, such as $R_{1,2}$ and $C_{1,2}$ which are the *mean* resistance and capacitance values associated with the bimodal peaks in $Z''(\omega)$. Based on these definitions, the principal cut-off frequency, $f_0 = 1/(R_1C_1)$, and the DC resistance, $Z(\omega = 0) = R_1 + R_2$, thus allowing R_2 to be calculated. Finally, C_2 can be derived using the secondary cut-off frequency, $f_0' = 1/(R_2C_2)$. All the extracted f_0, f_0', R and C values are given in Table 1. The extracted values of $R_{1,2}$ and $C_{1,2}$ are plotted as a function of annealing time, for ρ values of 0.5, 0.75 and 1.0 wt% (Fig.8). Since the precision of these fitted mean values is limited to an error of order 10%, only broad conclusions can be drawn. The mean resistances (Fig.8a) show that R_1 decreases markedly with annealing time (consistent with the raw data). The resistance components from the secondary distribution of relaxation times (R_2) are lower in comparison to R_1, typically 2 orders of magnitude lower. By contrast, the values of capacitance corresponding to C_1 and C_2 (Fig.8c) are similar in value and show no clear evidence of any systematic trend with increasing annealing time. Of additional importance, the measured DC capacitances of samples prior to annealing were all in the range of 10^{-10} to 10^{-9} F, as is broadly consistent with the values in Table 1. Furthermore, the real-part of the dielectric constant (ε_r) of samples generally has a similar magnitude before and after annealing (Fig. 4b, d).

We expect that any drastic changes in the ordering or morphology of CNTs during annealing would have had a significant and measureable effect on ε_r.

It is clear that the two relevant contributions to conductivity are, firstly, the formation of the percolating network and network topology and, secondly, the resistance between touching CNTs. Initially, the unannealed samples predominantly exhibit SWNT bundling, due to the colloidal mixing and freeze drying

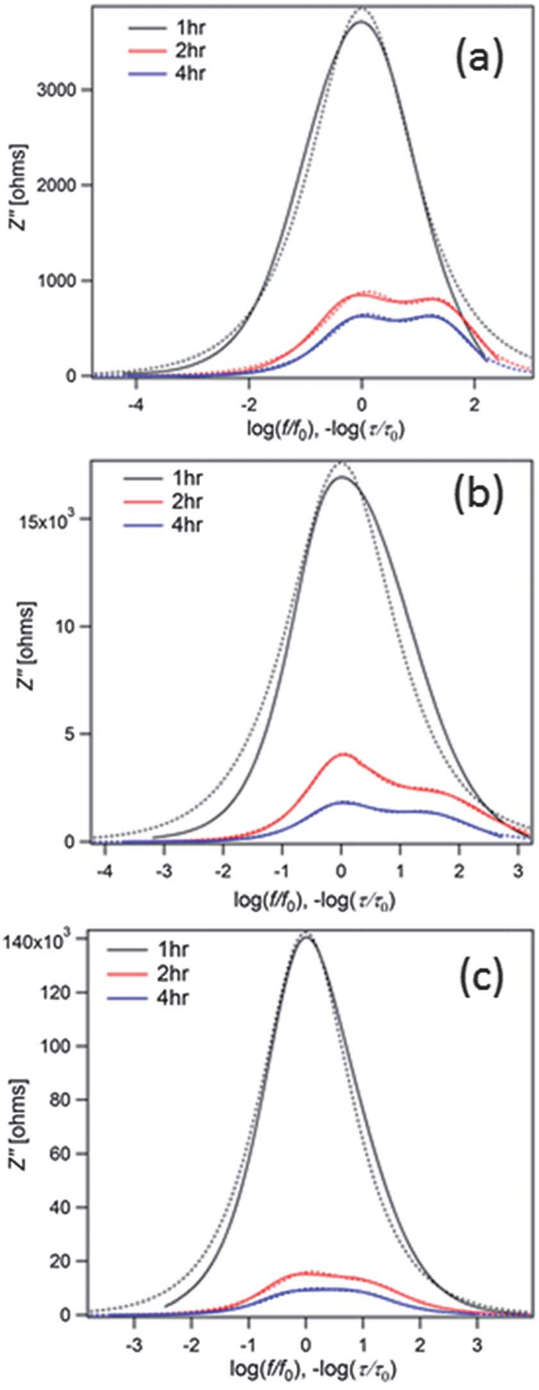

Fig. 7 Plots of imaginary Z *versus* log (f/f_0) for samples with (a) 1.0%, (b) 0.75% and (c) 0.5%wt SWNT, annealing times are as indicated. The dashed lines show fitting of the data to the model described in eqn (8).

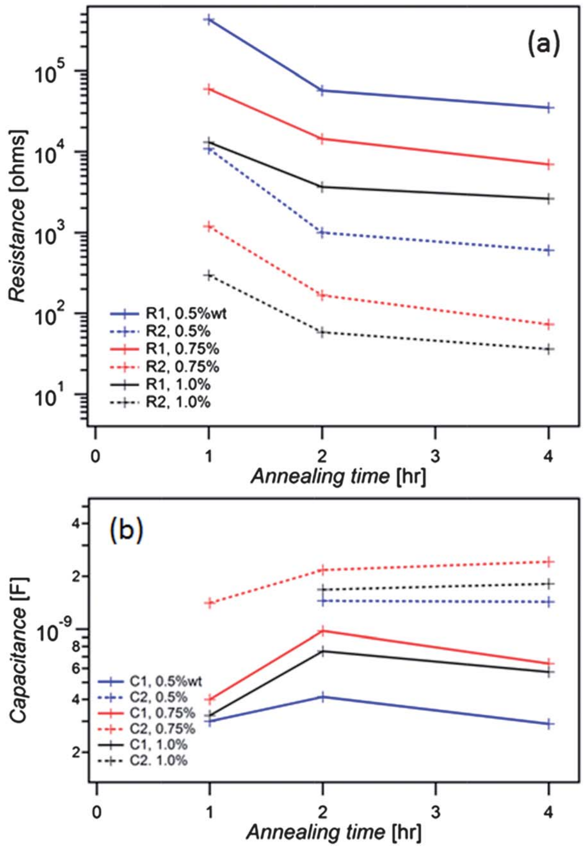

Fig. 8 Mean values of resistances R_1 and R_2 and capacitances C_1 and C_2, based on a bimodal distribution of relaxation times, as described in eqn (8). Data is shown as a function of annealing time, and SWNT concentrations are as indicated.

This journal is © The Royal Society of Chemistry 2012

Downloaded by University of Cambridge on 08 May 2012
Published on 08 May 2012 on http://pubs.rsc.org | doi:10.1039/C2SM06740D

processes. Two possible origins for resistance changes with annealing are identified; limited changes in the SWNT network topology due to the stabilizing effect of the surfactant being reduced (since reconfiguration is prevented by the rigid spheres, as confirmed by the TEM images), and changes in the contact resistances (most likely induced by thermal desorption of water from the surfactant layer, changing its surface conformation and thus the contact between SWNTs). During the initial stage of annealing, SWNTs can locally relax their bending strain in the now lower viscosity matrix which brings them more strongly into contact with each other (while remaining pinned by the rigid sphere cores); further studies are in progress to fully characterize and understand these relaxation mechanisms. The inter-tube (or inter-bundle) contact resistance is a very sensitive function of the physical tunnelling barrier between nanotubes.[46] As annealing continues, changes in the SDBS configuration on the surface reduce the contact resistance between SWNTs, as directly seen in the drop of R_1 with annealing time. However R_2 also drops as different parts of the SWNT network now regain electrical contact, reducing the average conducting SWNT chain lengths.

In previous reports, Garrett *et al.*,[44] modelled a SWNT-mat as a system of nanotube bundles and junctions in series, where the resistances and capacitances of these two distinct components could be analytically resolved. What is new here is the clearly observed separation into two distinct relaxation times in the SWNT opal impedance spectra. Whilst our SWNT-doped opals present a system of greater morphological complexity than in[44] they show a similar qualitative behaviour; the short relaxation time (low resistance) component emerging in impedance spectroscopy for >1 h annealing arises from shorter conducting SWNT lengths as multiply-connected sections rejoin the network when their junctions become conducting. The relatively constant capacitative contributions with increased annealing are also consistent with the apparent lack of any progressive morphological changes.

This suggests that assembly of SWNTs into heterogeneous polymer composites (such as these opals) can successfully proceed through solution assembly and any required processing, followed by local strain relaxation and electrical reconnection through controlled annealing. The use of opaline polymer composites acts also as a spectral indicator of local sub-micron morphologies during the SWNT processing, providing information that is extremely hard to access from other techniques (such as EM). Here, it confirms that large-scale network reorganisation (prevented in our topology by the locked sphere lattice) is not needed. It also allows the materials processing to be optimised for both electronic and optical functionality.

Mechanical properties (Young's modulus)

As a further complementary insight into the microscopic effects of the sample annealing process, and the mechanisms by which this influences conductivity, thin-film samples (as prepared) were characterized using stress/strain measurements to determine the elastic Young's modulus (see Fig. 9). A full description of the experimental method is given in the *Supporting Information*.†

A summary of the elasticity data, which was all measured in the low-strain limit well below the yield-point, is shown in Table 2. As expected, the samples with higher SWNT content are consistently measured to be more rigid than those with lower content (although only by a factor of around 2, when increasing the loading 5-fold from 0.1 to 0.5%wt SWNT). In all samples the measured modulus drops by around 50% on the initial 1 h annealing, indicating a softening. With increased annealing the composites then partially re-harden, but only by around 10% for the higher loaded sample. These measurements suggest that the SWNT network may indeed undergo a limited re-arrangement with annealing, particularly in the early stages up to 1 h, but not greatly afterwards. This provides further evidence that it is the contacts between SWNTs which change on annealing, in agreement with our earlier analysis of the impedance data.

In summary, whilst nanotube reptation in such a soft-matter composite may be possible,[47] we see no strong evidence for it in these experiments. Hence, we do not believe it plays a critical role in the increasing conductivity of samples with annealing.

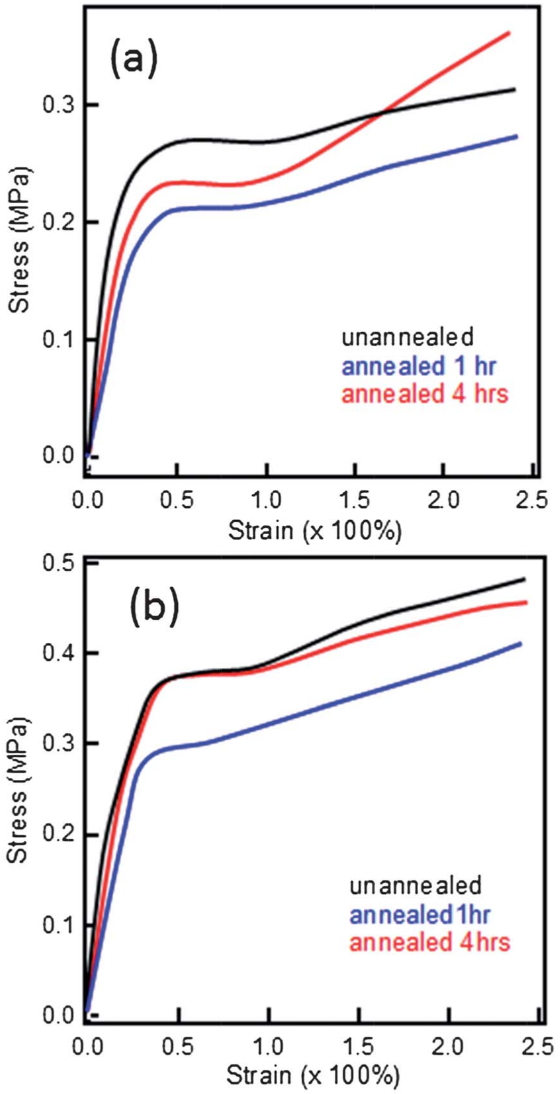

Fig. 9 Stress *vs.* strain plots for thin-film opal samples with SWNT loadings of (a) 0.1% and (b) 0.5% by weight. The annealing cycles (at 140 °C) of each sample are as indicated. Young's modulus is extracted from linear fits to the low strain limit.

Published on 08 May 2012 on http://pubs.rsc.org | doi:10.1039/C2SM06740D
Downloaded by University of Cambridge on 08 May 2012

Table 2 Young's modulus values (in units of MPa) for representative thin-film samples of different SWNT loading fraction and annealing time, as indicated. All samples were tested along the direction normal to the shear processing direction which controls the opaline self-assembly

wt% SWNT	Unannealed	1 h Anneal	4 h Anneal
0.1	1.93 ± 0.04	0.81 ± 0.01	1.24 ± 0.01
0.5	2.46 ± 0.02	1.60 ± 0.02	1.78 ± 0.01

Conclusions

Electrically conductive 3D photonic crystals, based on nanocomposites of SWNTs and polymeric opals, are demonstrated. These structures exhibit a strong iridescent color, indicating that the highly ordered opaline structures are not disrupted by the presence of the SWNT networks. Thermal annealing is found to cause a very significant improvement of the electrical conductivity of thin-film samples for SWNT loadings of over ~0.5 wt%. Our studies, using a combination of impedance spectroscopy and mechanical stress/strain characterization, suggest this is due to both improved nanotube network connectivity and also a lowering of the resistive component associated with inter-tube junctions. DC conductivities of the order of 10^{-4} S cm^{-1} are achieved, with percolation thresholds of less than 0.4 wt% of SWNT. We anticipate that further optimization of processing parameters, such as those of the sample annealing, will enable us to reach yet higher conductivities, making further practical applications feasible.

Our approach provides a distinctive route to combine the attractive optical and mechanical properties of polymeric opals[48–50] with intrinsic electro- and opto-electronic activity. Such advanced functionality can potentially lead to diverse applications, such as LEDs and electrically pumped photonic-crystal-feedback lasers (with inherent stretch tunability), electrochromic filters, optical sensors exploiting electrostriction effects,[51] or as components in light-harvesting and solar cell devices.

Acknowledgements

Y. I. and C. E. F. equally contributed to this work. This work was supported by UK EPSRC-GB Grants EP/G060649/1 and EP/E040241. Y.I. was supported by Excellent Young Researchers Oversea Visit Program from Japan Society for the Promotion of Science. C.E.F thanks Riccardo di Pietro, of the Cavendish Laboratory, for assistance with impedance spectroscopy measurements. The authors thank Prof U. Steiner, Dr Y. Y. Huang and Prof. E. M. Terentjev of the University of Cambridge for helpful discussions.

Notes and references

1 J. D. Joannopoulos, S. G. Johnson, J. N. Winn and R. D. Meade, *Photonic Crystals: Molding the Flow of Light*, Princeton University Press, Woodstock, UK 2008.
2 P. Vukusic, J. R. Sambles and C. R. Lawrence, *Nature*, 2000, **404**, 457.
3 C. E. Finlayson, F. Cattaneo, N. M. B. Perney, J. J. Baumberg, M. C. Netti, M. E. Zoorob, M. D. B. Charlton and G. J. Parker, *Phys. Rev. E*, 2006, **73**, 016619.
4 J. J. Baumberg, N. M. B. Perney, M. C. Netti, M. D. B. Charlton, M. Zoorob and G. J. Parker, *Appl. Phys. Lett.*, 2004, **85**, 354.
5 D. J. Norris and Y. A. Vlasov, *Adv. Mater.*, 2001, **13**, 371.
6 Y. N. Xia, B. Gates and Z. Y. Li, *Adv. Mater.*, 2001, **13**, 409.
7 O. L. J. Pursiainen, J. J. Baumberg, K. Ryan, J. Bauer, H. Winkler, B. Viel and T. Ruhl, *Appl. Phys. Lett.*, 2005, **87**, 101902.
8 O. L. J. Pursiainen, J. J. Baumberg, H. Winkler, B. Viel, P. Spahn and T. Ruhl, *Opt. Express*, 2007, **15**, 9553.
9 O. L. J. Pursiainen, J. J. Baumberg, H. Winkler, B. Viel, P. Spahn and T. Ruhl, *Adv. Mater.*, 2008, **20**, 1484.
10 J. Sussman, D. Snoswell, A. Kontogeoros, J. J. Baumberg and P. Spahn, *Appl. Phys. Lett.*, 2009, **95**, 173116.
11 J. J. Baumberg, O. L. Pursiainen and P. Spahn, *Phys. Rev. B*, 2009, **80**, 201103(R).
12 D. R. E. Snoswell, A. Kontogeorgos, J. J. Baumberg, T. D. Lord, M. R. Mackley, P. Spahn and G. P. Hellmann, *Phys. Rev. E*, 2010, **81**, 020401(R).
13 A. Kontogeorgos, D. R. E. Snoswell, C. E. Finlayson, J. J. Baumberg, P. Spahn and G. P. Hellmann, *Phys. Rev. Lett.*, 2010, **105**, 233909.
14 C. E. Finlayson, P. Spahn, D. R. E. Snoswell, G. Yates, A. Kontogeorgos, A. I. Haines, G. P. Hellmann and J. J. Baumberg, *Adv. Mater.*, 2011, **23**, 1540.
15 T. Ruhl and G. P. Hellmann, *Macromol. Chem. Phys.*, 2001, **202**, 3502.
16 T. Ruhl, P. Spahn and G. P. Hellmann, *Polymer*, 2003, **44**, 7625.
17 B. Viel, T. Ruhl and G. P. Hellmann, *Chem. Mater.*, 2007, **19**, 5673.
18 P. Spahn, C. E. Finlayson, W. Mbi Etah, D. R. E. Snoswell, J. J. Baumberg and G. P. Hellmann, *J. Mater. Chem.*, 2011, **21**, 8893.
19 S. Iijima and T. Ichihashi, *Nature*, 1993, **363**, 603.
20 P. M. Ajayan, L. S. Shadler, C. Giannaris and A. Rubio, *Adv. Mater.*, 2000, **12**, 750.
21 R. H. Baughman, A. A. Zakhidov and W. A. de Heer, *Science*, 2002, **297**, 787.
22 F. M. Du, R. C. Scogna, W. Zhou, S. Brand, J. E. Fischer and K. I. Winey, *Macromolecules*, 2004, **37**, 9048.
23 S. Barrau, P. Demont, A. Peigney, C. Laurent and C. Lacabanne, *Macromolecules*, 2003, **36**, 5187.
24 W. K. Hsu, V. Kotzeva, P. C. P. Watts and G. Z. Chen, *Carbon*, 2004, **42**, 1707.
25 O. Regev, P. N. B. El Kati, J. Loos and C. E. Koning, *Adv. Mater.*, 2004, **16**, 248.
26 N. Grossiord, J. Loos and C. E. Koning, *J. Mater. Chem.*, 2005, **15**, 2349.
27 S. V. Ahir, Y. Y. Huang and E. M. Terentjev, *Polymer*, 2008, **49**, 3841.
28 Y. Y. Huang and E. M. Terentjev, *Adv. Funct. Mater.*, 2010, **20**, 4062.
29 P. Goldberg-Oppenheimer, D. Eder and U. Steiner, *Adv. Funct. Mater.*, 2011, **21**, 1895.
30 T. Cassagneau and F. Caruso, *Adv. Mater.*, 2002, **13**, 34.
31 D. P. Puzzo, M. G. Helander, P. G. O'Brien, Z. Wang, N. Soheilnia, N. Kherani, Zhenghong Lu and Geoffrey A. Ozin, *Nano Lett.*, 2011, **11**, 1457.
32 B. White, S. Banerjee, S. O'Brien, N. J. Turro and I. P. Herman, *J. Phys. Chem.*, 2007, **111**, 13684.
33 N. Peng, Q. Zhang, S. Yuan, H. Li, J. Tian and L. Chan, *Nanotechnology*, 2007, **18**, 424035.
34 J. Chen, M. A. Hamon, H. Hu, Y. S. Chen, A. M. Rao, P. C. Eklund and R. C. Haddon, *Science*, 1998, **282**, 95.
35 J. Liu, A. G. Rinzler, H. Dai, J. H. Hafner, R. Bradley, P. J. Boul, T. Iverson, K. Shelimov, C. B. Huffman, F. Rodriguez-Macias, Y. Shon, T. R. Lee, D. T. Colbert and R. E. Smalley, *Science*, 1998, **280**, 1253.
36 O. Matarredona, H. Rhoads, Z. Li, J. H. Harwell, L. Balzano and D. E. Resasco, *J. Phys. Chem. B*, 2003, **107**, 13357.
37 H. Z. Geng, K. K. Kim, K. P. So, Y. S. Lee, Y. K. Chang and Y. H. Lee, *J. Am. Chem. Soc.*, 2007, **129**, 7758.
38 I. Alig, T. Skipa, D. Lellinger and P. Pötschke, *Polymer*, 2008, **49**, 3524.
39 Y. Y. Huang, T. P. J. Knowles and E. M. Terentjev, *Adv. Mater.*, 2009, **21**, 3945.
40 P. Pötschke, S. M. Dudkin and I. Alig, *Polymer*, 2003, **44**, 5023.
41 V. A. Gilchrist, J. R. Lu, E. Staples, P. Garrett and J. Penfold, *Langmuir*, 1999, **15**, 250.
42 J. R. Macdonald, *Impedance Spectroscopy*, Wiley, New York, USA, 1987.

This journal is © The Royal Society of Chemistry 2012

43 E. Bekyarova, M. E. Itkis, N. Cabrera, B. Zhao, A. Yu, J. Gao and R. C. Haddon, *J. Am. Chem. Soc.*, 2005, **127**, 5990.
44 M. P. Garrett, I. N. Ivanov, R. A. Gerhardt, A. A. Puretzky and D. B. Geohegan, *Appl. Phys. Lett.*, 2010, **97**, 163105.
45 R. M. Fuoss and J. G. Kirkwood, *J. Am. Chem. Soc.*, 1941, **63**, 385.
46 J. Wang, J. Sun, L. Gao, Y. Liu, Y. Wang, J. Zhang, H. Kajiura, M. Y-Li and K. Noda, *J. Alloys Compd.*, 2009, **485**, 456.
47 N. Fakhri, F. C. MacKintosh, B. Lounis, L. Cognet and M. Pasquali, *Science*, 2010, **330**, 1804.
48 C. Finlayson, C. Goddard, E. Papachristodoulou, D. Snoswell, A. Kontogeorgos, P. Spahn, G. Hellmann, O. Hess and J. J. Baumberg, *Opt. Express*, 2011, **19**, 3144.
49 P. V. Braun, *Nature*, 2011, **472**, 423.
50 C. E. Finlayson, A. I. Haines, D. R. E. Snoswell, A. Kontogeorgos, S. Vignolini, J. J. Baumberg, P. Spahn and G. P. Hellmann, *Appl. Phys. Lett.*, 2011, **99**, 261913.
51 Q. Zhao, A. I. Haines, D. R. E. Snoswell, C. Keplinger, R. Kaltseis, S. Bauer, I. Graz, R. Denk, P. Spahn, G. Hellmann and J. J. Baumberg, *Appl. Phys. Lett.*, 2012, **100**, 101902.

Published on 08 May 2012 on http://pubs.rsc.org | doi:10.1039/C2SM06740D
Downloaded by University of Cambridge on 08 May 2012